Research Square

Preprints are preliminary reports that have not undergone peer review.
They should not be considered conclusive, used to inform clinical practice,
or referenced by the media as validated information.

Mechanical properties and acoustic emission characteristics of fissured shale under true triaxial unloading and reloading

Beiyi Dong
Shijiazhuang Tiedao University
Xinqiang Gao
gaoxinqiang@stdu.edu.cn
Shijiazhuang Tiedao University
Dongliang Ji
Shijiazhuang Tiedao University
Chao Kong
Southwest University of Science and Technology
Qian Yan
Shijiazhuang Tiedao University
Minghao Ruan
Shijiazhuang Tiedao University

Article

Keywords: acoustic emission, failure characteristics, fissured shale, mechanical properties, true triaxial testing, unloading–reloading

Posted Date: November 10th, 2026

DOI: https://doi.org/10.21203/rs.3.rs-11456607/v1

License: This work is licensed under a Creative Commons Attribution 4.0 International License.
Read Full License

Additional Declarations: No competing interests reported.

Mechanical properties and acoustic emission characteristics of fissured shale under true triaxial unloading and reloading

Beiyi Dong[1,2], Xinqiang Gao[1,2,3]*, Dongliang Ji[1,3], Chao Kong[4], Qian Yan[1], Minghao Ruan[1,2]

1.*State Key Laboratory of Mechanical Behavior and System Safety of Traffic Engineering Structures, Shijiazhuang Tiedao University, Shijiazhuang 050043, China*

2.School of Civil Engineering, Shijiazhuang Tiedao University, Shijiazhuang 050043, China

3.Hebei Key Laboratory of Mechanics Behavior Evolution and Control of Transport Engineering Structures, Shijiazhuang 050043, China

4.School of Civil Engineering and Architecture, Southwest University of Science and Technology, Mianyang 621000, China

*Corresponding author, Professor, E-mail: gaoxinqiang@stdu.edu.cn

Abstract: Excavation unloading and subsequent support affect the stability of fissured rock around tunnels. True triaxial unloading and reloading tests were conducted on shale specimens with different fissure inclinations, numbers, and configurations. Acoustic emission (AE) counts and energy were monitored throughout testing. At a fissure inclination of 45°, increasing fissure number from zero to three reduced peak strength from 119.4 to 44.7 MPa and elastic modulus from 12.06 to 4.72 GPa. Three failure processes were identified: a stress drop followed by recovery and failure, failure without a distinct preceding drop, and a drop coinciding with failure. Unloading strain in the minor principal stress direction was approximately two to five times that in the major principal stress direction. AE activity increased sharply near failure, whereas cumulative counts decreased as fissure configurations became more complex. Bedding promoted interlayer cracking and influenced crack propagation. Adding a third fissure increased the failure angle from 61° to approximately 76° and intensified fragmentation. These results indicate that fissure geometry, rock bridge continuity, and bedding jointly control shale deformation and failure. The findings provide experimental evidence for stability assessment, support design, and damage monitoring in fractured shale tunnels.

Keywords: acoustic emission; failure characteristics; fissured shale; mechanical properties; true triaxial testing; unloading–reloading

1. Introduction

Transport infrastructure is expanding into increasingly complex geological settings. Tunnels therefore encounter fractured rock that contains fissures, bedding planes, and other discontinuities [1]. Excavation unloading and subsequent support can promote fissure growth and coalescence, which may trigger geological hazards [2, 3]. Understanding the response of fissured rock to unloading and reloading is therefore essential for tunnel stability assessment.

Excavation unloading can substantially reduce rock strength. Lu et al. [4] combined theoretical analysis with field measurements and showed that load release during blasting is transient under moderate and high in situ stress. The reported unloading duration was about 10–100 ms. The resulting vibration may exceed that caused by the blast load and may control the surrounding rock response. Zhang et al. [5] found that transient unloading generates dynamic tensile stress around deep tunnels. Shorter unloading durations produced larger tensile zones and more extensive cracking. Cracking depth increased with the lateral pressure coefficient, and the damaged zone formed a V shape. Ding et al. [6] simulated vertical loading with radial unloading on one face. Higher unloading rates and gas pressures reduced coal strength, increased AE activity, and advanced failure precursors. Failure propagated inward from the unloaded face through several shear bands. Rong et al. [7] compared the true triaxial response of sandstone under several unloading paths. Unloading with increasing axial stress caused greater strain energy release and more violent failure. Unloading with decreasing axial stress produced a more gradual response. The deformation modulus decreased during unloading, while Poisson's ratio rose rapidly. Xu et al. [8] reproduced energy accumulation and stress concentration failure. At the same confining pressure, unloading strength was about 80% of loading strength. Hou et al. [9] developed a small specimen system that reproduced the unloading path and rate associated with roadway excavation.

Many studies have examined the effect of fissures on rock failure. Wong and Einstein [10] identified seven crack types in uniaxial tests on gypsum and marble with a single fissure. Yang and Jing [11] identified nine crack types in sandstone and tracked their growth with photography and AE monitoring. Wang et al. [12] conducted biaxial tests on specimens with different initial crack shapes and inclinations. Wing cracks propagated parallel to the free surfaces above a threshold biaxial load ratio, but their growth was restricted below that threshold. Pakzad et al. [13] combined conventional triaxial

tests with numerical simulations. Confinement increased peak strength at every tested fissure inclination, and the trend was associated with damage before peak stress.

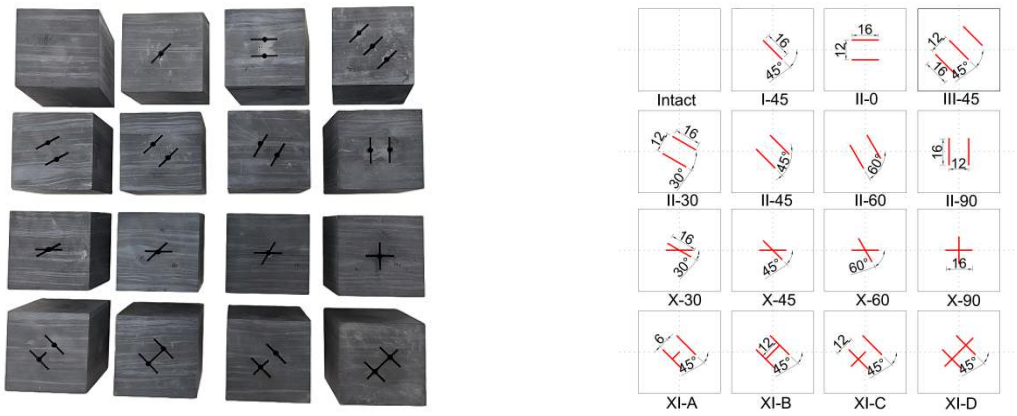
Most previous experiments used uniaxial, biaxial, or conventional triaxial loading, although rock in situ is subjected to a three dimensional stress state. True triaxial tests have therefore been used to study fissured rock under more representative loading conditions [14–16]. Chang et al. [17] tested sandstone with a single fissure. Shear cracks were much more common than tensile cracks, and the authors proposed a damage model that included microscopic damage. Yang et al. [18] identified ten characteristic crack types in true triaxial tests on sandstone with a single fissure.

The response of fissured shale to true triaxial unloading and reloading remains insufficiently understood. In particular, the roles of fissure inclination, configuration, and rock bridge continuity require further study. This work examined shale from the fractured rock surrounding the Yangjiawan Tunnel in Yunnan. The test program varied fissure inclination, number, and configuration under a true triaxial unloading–reloading path. AE monitoring was used to relate stress–strain behavior, strength, unloading strain, and final crack patterns to the damage process. The results provide experimental evidence for stability assessment and support design in tunnels excavated through fractured rock.

2. Experimental equipment and procedures

2.1 Specimen preparation

Shale was collected from the Yangjiawan Tunnel on the Yongshan connecting road of the expressway between Xinshi, Yibin, and Panzhihua (Fig. 1). Cubic specimens measured 50 mm × 50 mm × 50 mm. The deviation from parallelism between opposite faces did not exceed 0.05 mm. Each fissure was about 17 mm long, equal to one third of the specimen edge length, and 1 mm wide [19]. Five configurations were prepared: one fissure (I-45), two parallel fissures (Group II), two conjugate fissures (Group X), three parallel fissures (III-45), and three intersecting fissures (Group XI). The fissures in I-45 and III-45 were inclined at 45° to bedding. Group II contained inclinations of 0°, 30°, 45°, 60°, and 90° relative to bedding. In Group X, one fissure was parallel to bedding and the other was inclined at 30°, 45°, 60°, or 90°. Group XI was produced by adding a third fissure perpendicular to the parallel fissures in II-45. The four arrangements represented intersections of 25% in XI-A, 50% in XI-B and XI-C, and 100% in XI-D. XI-B and XI-C had different intersection geometries. All fissures extended through the full specimen thickness.



(a) Specimen photographs (b) Fissure geometries/mm

Figure 1. Shale specimens and fissure geometries. Dimensions in mm.

All specimens were obtained from blocks collected at the same tunnel location to reduce material heterogeneity. Pencil lead break tests were performed on three adjacent faces to screen for hidden cracks (Fig. 2). Each face was tested three times, giving nine measurements per specimen. Specimens with large differences in P wave velocity were excluded. Table 1 gives the measurements for the intact specimen. The mean velocity parallel to bedding was 5596 m/s. The corresponding values normal to bedding were 4715 and 4644 m/s. Bedding therefore reduced P wave velocity by about 16%.

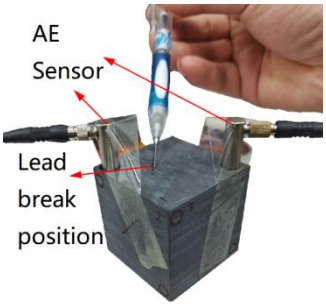


Figure 2. Pencil lead break test.

Table 1. P wave velocities measured during specimen screening.

Test face	Test no.	P wave velocity, v (m/s)	Mean P wave velocity, v_a (m/s)
Face 1 (parallel to bedding)	1	5333	5596
	2	5629	
	3	5827	
Face 2 (perpendicular to bedding)	1	4610	4715
	2	4713	
	3	4822	
Face 3 (perpendicular to bedding)	1	4713	4644
	2	4610	
	3	4610	

2.2 Testing system

True triaxial unloading–reloading tests were conducted with the DRTB-3000 rock disturbance testing system (Fig. 3). The system applies rigid loading in three orthogonal directions and has a frame stiffness of 6 GN/m. Linear variable differential transformers measured specimen deformation. Interlocking platens covered the specimen faces and reduced unloaded corner regions [20]. The maximum loads were 3000 kN in the Z and Y directions and 1000 kN in the X direction. Sinusoidal, half sinusoidal, square wave, and other disturbance loads can be applied at 0–10 Hz with a maximum displacement amplitude of 0.5 mm. A ten channel PXDAQ system recorded AE ring down counts, energy, and related parameters throughout each test.

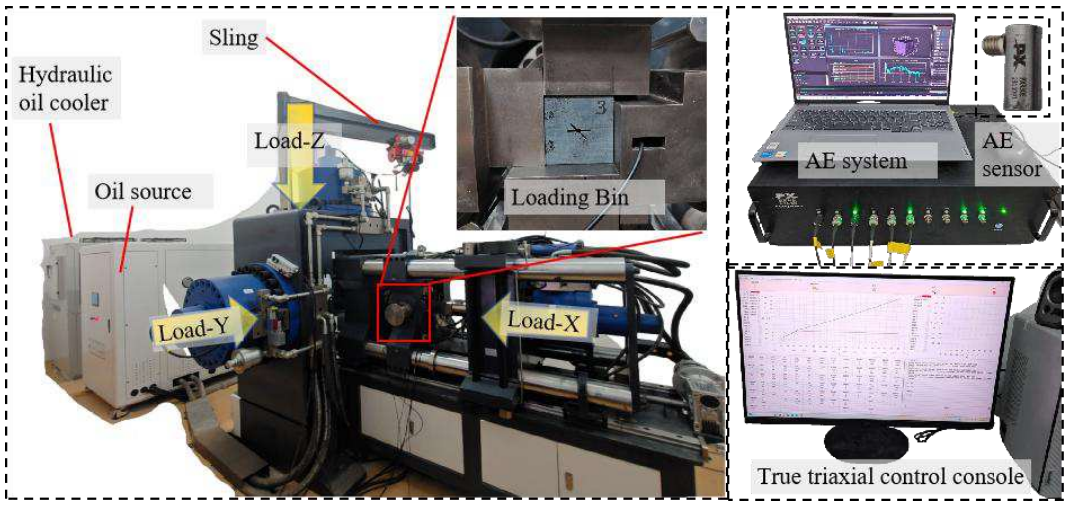


Figure 3. DRTB-3000 true triaxial rock disturbance testing system.

2.3 Loading procedure

The Z, Y, and X axes corresponded to the major, intermediate, and minor principal stress directions, denoted by σ_1, σ_2, and σ_3. At the sampling location, the maximum horizontal in situ stress ranged from 6.09 to 20.86 MPa. The minimum horizontal stress ranged from 3.92 to 13.17 MPa. The stresses before unloading were therefore set to $\sigma_1 = 30$ MPa, $\sigma_2 = 20$ MPa, and $\sigma_3 = 15$ MPa. Figure 4 shows the stress path. The major principal stress direction was normal to bedding, while the minor principal stress direction was normal to the fissure faces. All three stresses were increased at 6 MPa/min to their target values and held for 30 s. The minor principal stress was then reduced from 15 to 0 MPa at 6 MPa/min to simulate excavation. After a 30 s hold, σ_3 was raised to 0.5 MPa at the same rate to represent initial support [21]. This value is a simplified representation of support confinement and does not represent a uniform field pressure. With σ_2 and σ_3 held at 20 and 0.5 MPa, σ_1 was increased under displacement

control at 0.1 mm/min until failure. This final stage represented tangential stress concentration after excavation. Table 2 lists the specimen groups.

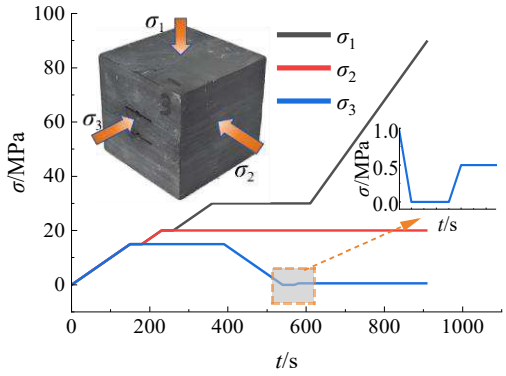


Figure 4. Stress path for the true triaxial tests.

Figure 5 shows representative loading photographs and the AE sensor arrangement. A central hole in each relevant platen allowed the sensor to contact the specimen directly. Couplant was applied at the sensor and rock interface. The effect of the sensor holes on specimen behavior was neglected. The sampling frequency was 1 MHz, and the threshold was 60 dB. The event definition time was 2000 μs, the lockout time was 100 ms, and the over location setting was 100 ms. The preamplifier gain was 100.

Table 2. Fissured shale specimens used in the true triaxial unloading–reloading tests.

Specimen	Dimensions (mm × mm × mm)	Inclination (°)	Mass (g)	Density (kg/m³)
II-0	50.24 × 50.16 × 50.22	0	327.1	2624.44
II-30	50.21 × 50.29 × 50.15	30	327.7	2627.66
II-45	50.11 × 50.13 × 49.94	45	323.8	2621.23
II-60	50.04 × 50.08 × 50.06	60	324.4	2626.07
II-90	50.05 × 50.13 × 50.30	90	326.9	2630.29
I-45	50.24 × 50.28 × 50.28	45	332.8	2640.21
III-45	50.21 × 50.27 × 50.24	45	324.8	2620.86
X-30	50.22 × 50.29 × 50.22	30	329.8	2640.22
X-45	50.21 × 50.13 × 50.13	45	328.4	2642.88
X-60	50.30 × 50.25 × 50.21	60	330.0	2640.22
X-90	50.14 × 50.27 × 50.31	90	329.4	2637.56
XI-A	50.18 × 50.10 × 50.21	-	326.4	2633.34
XI-B	50.16 × 50.13 × 50.16	-	324.8	2630.21
XI-C	50.13 × 50.13 × 49.89	-	322.5	2627.62

Specimen	Dimensions (mm × mm × mm)	Inclination (°)	Mass (g)	Density (kg/m³)
XI-D	49.98 × 50.13 × 50.15	-	321.8	2631.43
Intact	50.10 × 50.12 × 50.12	-	330.0	2622.13

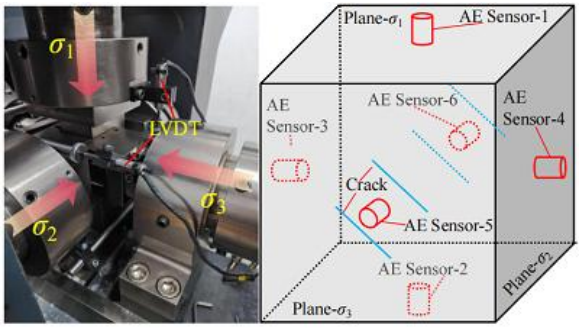


Figure 5. Representative loading photographs and AE sensor positions.

3. Mechanical behavior

3.1 Stress–strain behavior

The intact specimen reached a peak strength of about 120 MPa (Fig. 6). A distinct yield plateau developed after peak stress, followed by rapid failure. Volumetric strain first increased and then became negative. The specimen therefore compacted after unloading and reloading, then dilated near and after peak stress.

Figures 7–9 show the stress–strain curves for each fissure configuration. The symbols ε_1, ε_2, and ε_3 denote strain in the major, intermediate, and minor principal stress directions. The symbol ε_v denotes volumetric strain.

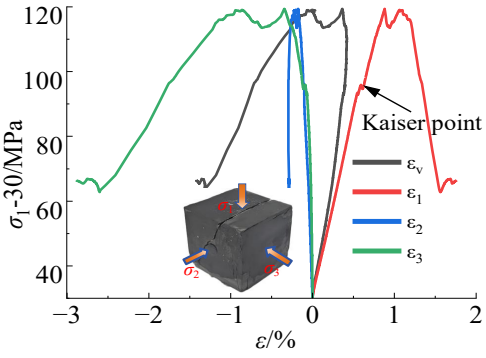
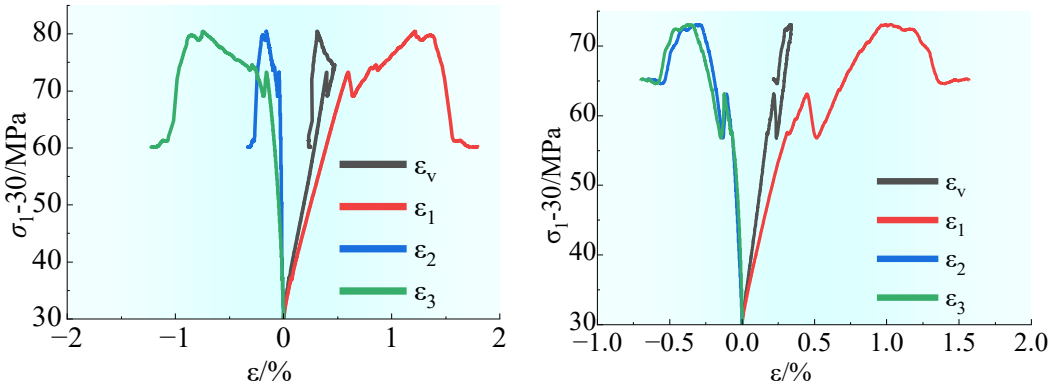


Figure 6. Stress–strain curves of the intact specimen.

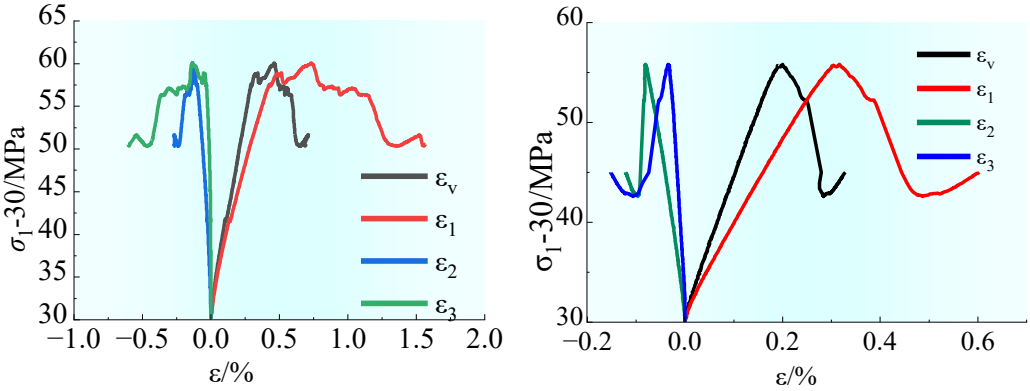
3.1.1 Group II

The specimens with parallel fissures passed through similar deformation stages: compaction, elastic deformation, fissure closure, and failure (Fig. 7). Fissure closure appeared as a stress drop. Specimens with inclinations up to 45° had a clear yield plateau that was longer than that of the intact

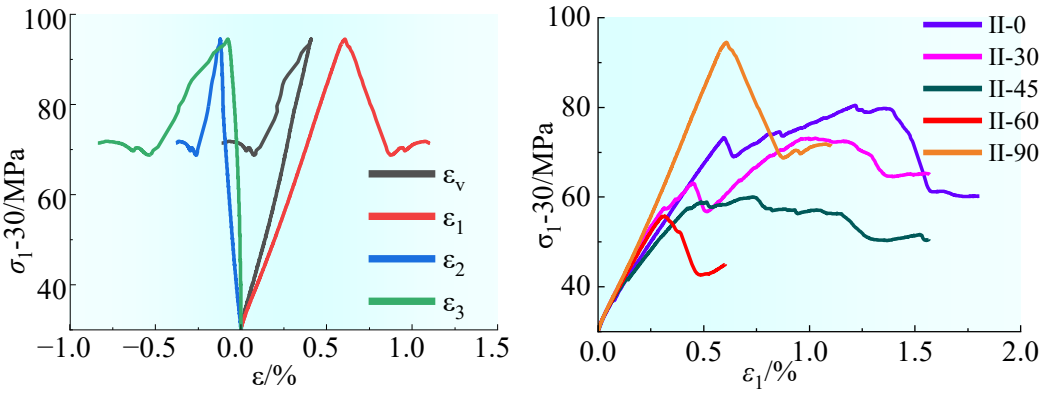
specimen. At larger inclinations, the plateau was shorter and fissure closure merged with failure. Failure became more abrupt with increasing inclination. The curves became steeper, and plastic deformation was less developed. Sliding along the fissure surfaces also shortened the time to failure. The specimens at 0° and 30° compacted and then dilated slightly. The specimens at 45° and 60° compacted throughout loading, while the specimen at 90° compacted and then dilated. Thus, the volumetric response changed systematically with inclination. At 0°, the rock bridge was widest in the intermediate principal stress direction and narrowest in the major principal stress direction. The opposite geometry occurred at 90°. These observations indicate that bridge width in the major principal stress direction strongly influenced volumetric deformation.



(a) II-0 (b) II-30



(c) II-45 (d) II-60

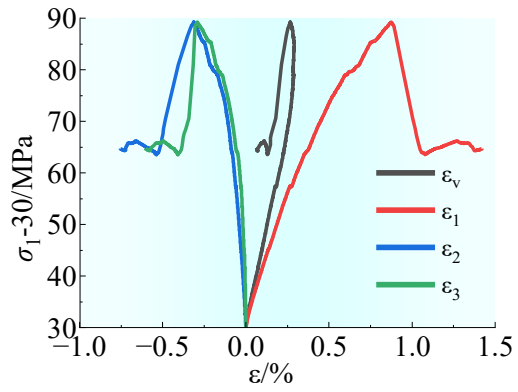


(e) II-90 (f) Major principal stress–strain curves

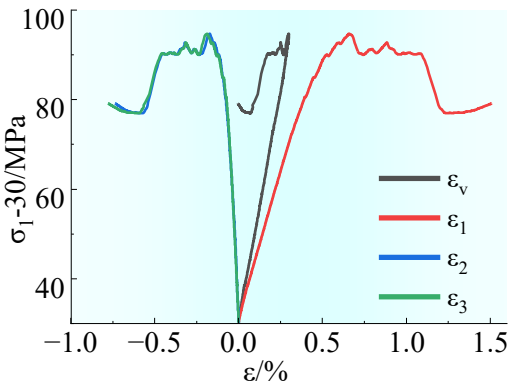
Figure 7. Stress–strain curves of Group II.

3.1.2 Group X

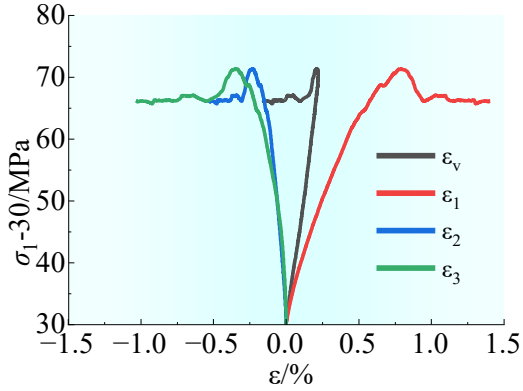
The conjugate fissure specimens showed similar stages of compaction, elastic deformation, plastic deformation, and failure (Fig. 8). A stress drop preceded failure, and its magnitude decreased with inclination. Stress fell from 90 to 63 MPa at 30°, from 90 to 78 MPa at 45°, and from 73 to 67 MPa at 60°. No distinct drop occurred at 90°. Horizontal bridge width in the intermediate principal stress direction also decreased with inclination. This agreement suggests that horizontal bridge width influenced the stress drop. All specimens compacted and then dilated as σ_1 increased. X-30 showed a steep drop and limited plastic deformation, whereas X-45 developed a clear yield plateau.



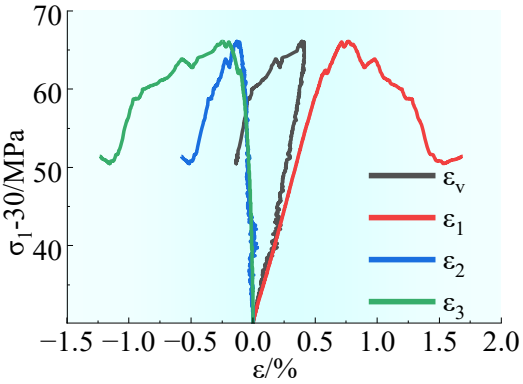
(a) X-30



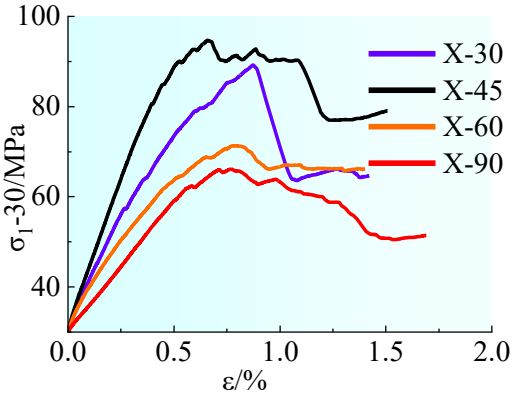
(b) X-45



(c) X-60



(d) X-90



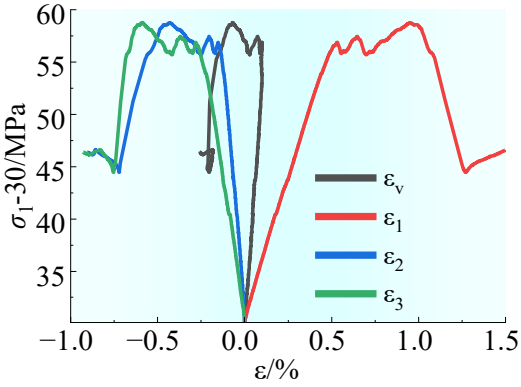
(e) Major principal stress–strain curves

Figure 8. Stress–strain curves of Group X.

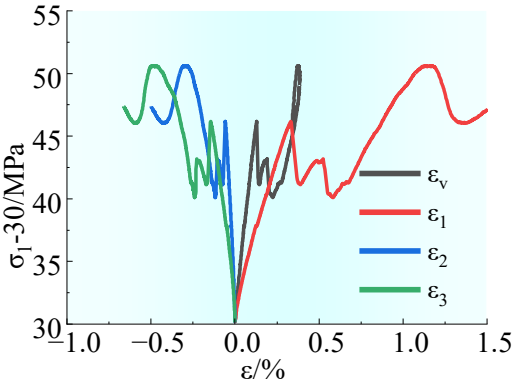
3.1.3 Group XI

After displacement controlled loading began, the Group XI specimens passed through a short elastic stage and rapidly entered plastic deformation (Fig. 9). Their rising curves were slightly convex and nonlinear. XI-A compacted and then dilated, whereas the other specimens compacted throughout loading. XI-A and XI-B developed W shaped yield plateaus. This response indicates progressive fissure

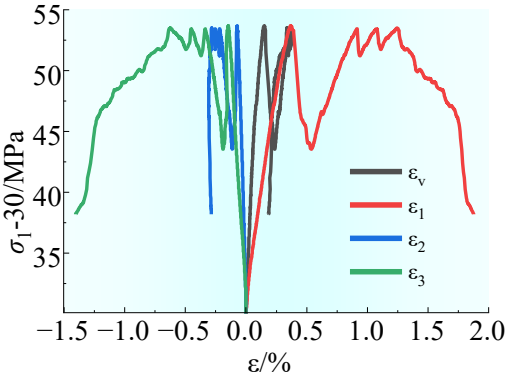
closure and relatively developed plastic deformation. XI-C and XI-D showed larger stress drops of about 10 MPa and less plastic deformation.



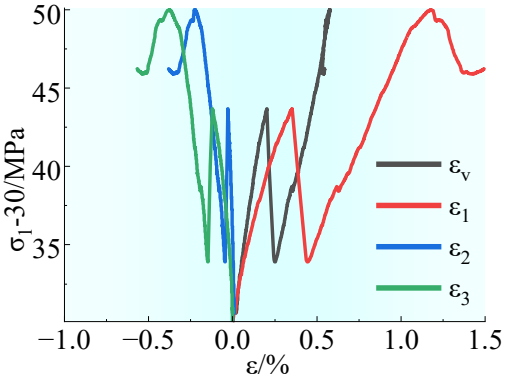
(a) XI-A



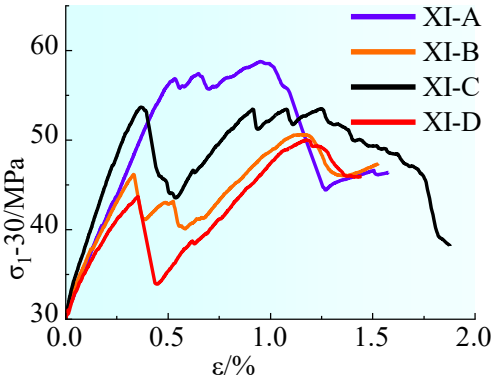
(b) XI-B



(c) XI-C



(d) XI-D



(e) Major principal stress–strain curves

Figure 9. Stress–strain curves of Group XI.

3.1.4 Comparison among configurations

Under the same stress path and at a fissure inclination of 45°, the intact, one fissure, two fissure, and three fissure specimens reached about 120, 100, 60, and 45 MPa. Their normalized peak strengths were 1.000, 0.833, 0.500, and 0.375. Peak strength therefore decreased as the number of fissures

194 increased. Additional fissures reduced the intact matrix available for load transfer and increased local
195 stress at fissure tips and rock bridges. Unloading σ_3 also reduced normal confinement on the fissure
196 surfaces. This condition promoted opening, frictional sliding, and local bridge failure during later
197 loading. Earlier studies reported similar effects of fissure interaction and bridge coalescence on crack
198 paths and peak strength [17–19].

199 Some specimens showed an abrupt stress drop followed by recovery before final failure. In Group
200 II, this response occurred at inclinations of 45° or less. At larger inclinations, the drop coincided with
201 failure. The response was weaker in Group X. Only X-30 showed a drop that coincided with failure,
202 while the other specimens had little or no distinct drop. In Group XI, the drops reached about 10 MPa.
203 Repeated drops sometimes produced W shaped curves. Plastic deformation was most gradual in Group
204 X and most abrupt in Group XI. Group II showed an intermediate response.

205 The normalized stress drop ratio was defined as

206 $$D = \frac{\sigma_{\text{pre-drop}} - \sigma_{\min}}{\sigma_p} \tag{1}$$

207 where σ_{pre} is the local stress maximum immediately before a distinct drop, σ_{min} is the local
208 minimum after the drop, and σ_p is peak strength. All stresses are expressed in MPa.

209 The interval between the stress drop and failure was defined as

210 $$\Delta t = t_f - t_{\min} \tag{2}$$

211 where t^f is the time of macroscopic failure and t_{min} is the time at the minimum stress after the drop.
212 Both quantities are expressed in seconds.

213 Table 3 gives the normalized stress drop ratios and time intervals calculated from Eqs. (1) and (2).
214 Three failure processes were identified. Type 1 comprised a stress drop, recovery, and later failure, with
215 $D \geq 2\%$. Type 2 showed no distinct drop before failure and had $D < 2\%$. In Type 3, the only major drop
216 coincided with failure and Δt was less than 20 s. XI-A showed Type 2 behavior, while the other Group
217 XI specimens showed Type 1 behavior. In Group II, inclinations below 60° produced Type 1 behavior,
218 and inclinations of 60° or more produced Type 3 behavior. I-45, III-45, X-60, and X-90 showed Type 2
219 behavior. X-30 showed Type 3 behavior, and X-45 showed Type 1 behavior. The short warning interval
220 associated with Type 3 may be relevant to instability assessment.

Table 3. Classification of specimen failure processes.

Failure process	ID	Stress-drop ratio D (%)	Time to failure Δt (s)	Pre-failure drop
Type 1 Drop, recovery, then failure	II-0	4.3	274	Large
	II-30	5.3	281	Large
	II-45	2.1	155	Large
	X-45	3.9	118	Large
	XI-B	4.1	316	Large
	XI-C	7.8	385	Large
	XI-D	8.0	334	Large
Type 2 No distinct pre-failure drop	I-45	0.5	125	Small
	III-45	0.7	54	Small
	XI-A	1.4	130	Small
	X-60	0.1	81	Small
	X-90	1.1	115	Small
Type 3 Drop coinciding with failure	II-60	10.9	19	None
	II-90	21.5	16	None
	X-30	21.8	17	None

Note: For Type 3 specimens, D was calculated from the stress drop at failure. For the other specimens, the largest drop before failure was used. The qualitative magnitude describes the largest drop before the final failure drop.

3.2 Strength and deformation parameters

Peak strength generally decreased as fissure number increased across Groups I, II, and III (Fig. 10). It also decreased as the configuration became more complex across Groups I, II, and XI. Peak strength varied within a narrow range in Group XI.

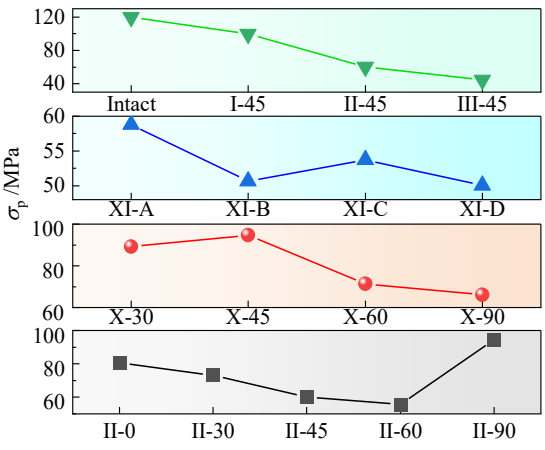


Figure 10. Peak strength of each specimen.

The first comparison included the intact specimen, I-45, II-45, and III-45. Peak strength decreased from 120 MPa in the intact specimen to 100, 60, and 45 MPa as fissures were added. The corresponding reductions were about 16.7%, 50.0%, and 62.5%. In Group XI, rock bridge continuity was associated

with peak strength. XI-A and XI-C retained part of the bridge and were stronger than XI-B and XI-D, where the bridge was cut through. Between the latter specimens, the X shaped intersection gave a slightly lower strength than the T shaped intersection. The upper and lower parallel fissures are referred to as the first and second fissures. The third fissure intersected the second at 90°. Within these tests, bridge continuity had a greater influence than the X or T intersection shape. In Group X, peak strength first increased and then decreased as inclination rose from 30° to 90°. It was highest at 45° (95 MPa) and lowest at 90° (66 MPa), a reduction of about 30.5%. Group II showed the opposite trend. Peak strength was highest at 90° (95 MPa) and lowest at 60° (56 MPa), a difference of about 41.1%.

Normalized peak strength was defined as

$$\eta_\sigma = \sigma_{p,fra} / \sigma_{p,\text{int act}} \tag{3}$$

where σ_p,^{f} is the peak strength of a fissured specimen and $\sigma_{p,i}$ is that of the intact specimen. Both quantities are expressed in MPa.

The strength reduction ratio was defined as

$$R_\sigma = 1 - \eta_\sigma \tag{4}$$

Figures 11 and 12 show the normalized peak strength and strength reduction ratio obtained from Eqs. (3) and (4). Both measures showed an approximately linear trend with fissure number. Normalized strength decreased, while the reduction ratio increased. The range of normalized strength within Group XI was less than 0.1. In Group X, normalized strength first increased and then decreased with inclination. The reduction ratio showed the opposite trend, with a turning point near 45°. Group II showed a reverse pattern, with a turning point near 60°. At this inclination, normalized strength was lowest and the reduction ratio was highest.

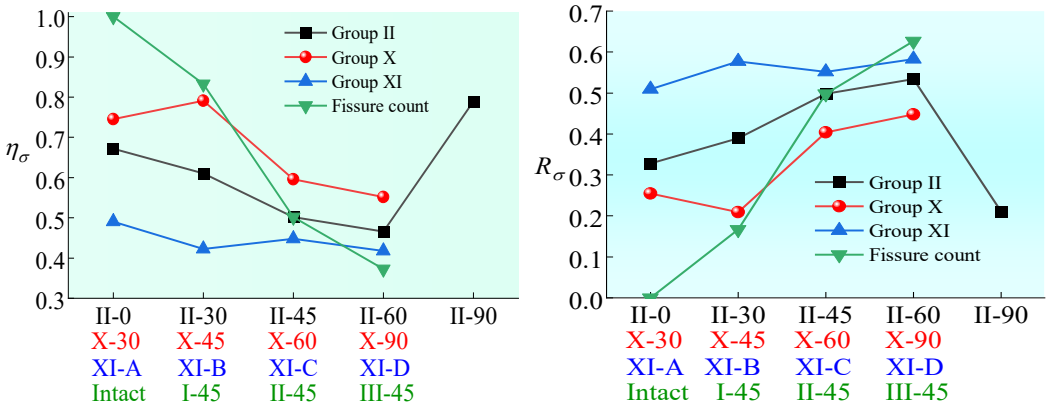


Figure 11. Normalized peak strength. Figure 12. Strength reduction ratio.

Table 4 lists peak strain $\Delta\varepsilon_{1,p}$, elastic modulus E_1, residual strength σ_r, and directional Poisson's ratios during final loading in the major principal stress direction. Peak strain was measured from the start of this stage. The ratios μ_{12} and μ_{13} relate strain in the intermediate and minor principal stress directions to strain in the major principal stress direction.

At a fissure inclination of 45°, increasing the fissure number from zero to three reduced the elastic modulus from 12.06 to 9.53, 6.13, and 4.72 GPa. Peak strain decreased overall from 0.88% to 0.46%. Residual strength decreased from 65.9 to 38.7 MPa. Multiple fissures therefore reduced stiffness and the deformation capacity before peak stress. They also reduced strength after peak stress. I-45 was an exception, with a residual strength of 74.7 MPa. Residual capacity did not decrease linearly with fissure number and also depended on closure and frictional sliding.

Table 4. Mechanical parameters of the specimens.

Specimen	**$\Delta\varepsilon_{1,p}$ (%)**	**E_1 (GPa)**	**σ_r (MPa)**	**μ_{12}**	**μ_{13}**
Intact	0.88	12.06	65.9	0.25	0.2
I-45	0.90	9.53	74.7	0.24	0.2
II-45	0.73	6.13	51.1	0.24	0.1
III-45	0.46	4.72	38.7	0.23	0.3
II-0	1.21	7.02	60.2	0.05	0.3
II-30	1.03	7.79	65.2	0.23	0.3
II-60	0.31	8.47	44.2	0.26	0.1
II-90	0.61	11.22	71.7	0.21	0.1
X-30	0.87	7.05	64.6	0.24	0.2
X-45	0.66	12.77	78.7	0.21	0.2
X-60	0.78	6.07	66.1	0.25	0.4
X-90	0.77	6.02	51.2	0.04	0.2
XI-A	0.95	5.04	46.2	0.28	0.4
XI-B	1.14	4.42	47.1	0.17	0.5
XI-C	0.36	6.98	39.5	0.20	0.5
XI-D	1.17	3.26	45.9	0.12	0.4

The effect of inclination depended on fissure configuration. II-60 had a peak strain of 0.31% and a residual strength of 44.2 MPa. Its large unloading strain suggests that deformation during unloading reduced part of the capacity available during final loading. X-60 had an elastic modulus of 6.07 GPa, while μ_{13} reached 0.420 and the residual strength ratio reached 0.927. This specimen combined strong lateral strain coupling with high residual capacity. The response near 60° was therefore specific to fissure configuration rather than a universal threshold.

In Group XI, μ_{13} was about 1.6–3.1 times μ_{12}. Deformation was therefore stronger in the minor principal stress direction. This result agrees with the directional asymmetry in unloading strain.

The position of the third fissure in Group XI altered peak strength, stress drops, and final crack paths. A continuous bridge allowed load transfer through the intact matrix. A larger projected intersection reduced the effective bridge length and promoted stress concentration at fissure tips, intersections, and remaining bridges. Local bridge failure may have transferred load to the adjacent matrix and produced recovery after a stress drop. Repeated drops and recoveries are consistent with sequential bridge failure and redistribution of the load path. Internal imaging would be required to verify this interpretation.

3.3 Unloading strain

Unloading strain was used to describe the immediate deformation of fissured rock after excavation. Figure 13 shows the absolute strains in the major and minor principal stress directions. Strain in the intermediate principal stress direction was below 10^{-4} and showed no appreciable change.

Unloading strain in the minor principal stress direction was about two to five times that in the major principal stress direction. Both measures followed similar overall trends, with local differences. They increased with fissure number across the intact, I-45, II-45, and III-45 specimens.

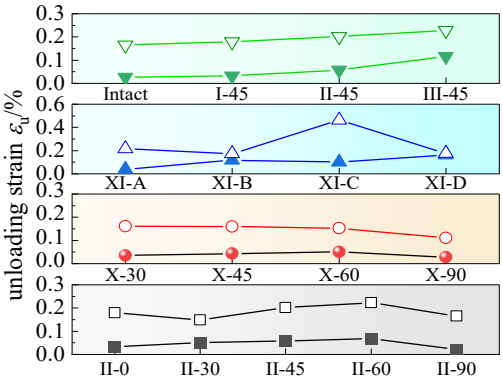


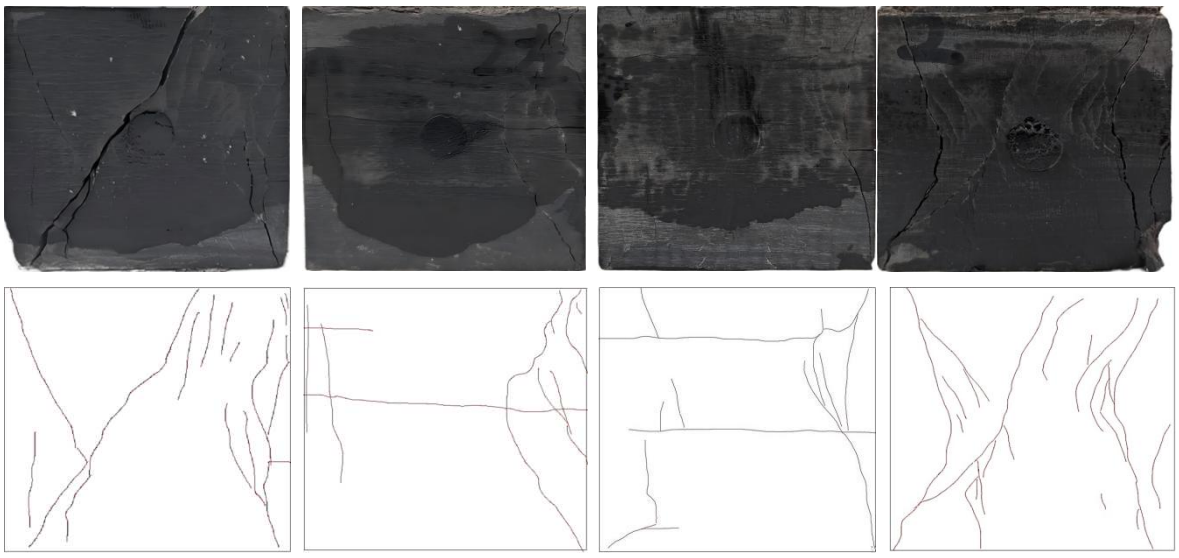
Figure 13. Unloading strain. The symbol ε_u denotes unloading strain. (Open symbols show the major principal stress direction, and filled symbols show the minor principal stress direction)

In Group XI, unloading strain in the major principal stress direction increased with rock bridge connectivity. Minor direction strain changed markedly in XI-C but varied little among the other specimens. In Group X, minor direction strain decreased with inclination, with a larger reduction at 60°. Major direction strain first increased and then decreased, reaching its maximum at 60°. In Group II, minor direction strain decreased to 30°, increased to 60°, and then decreased again. Major direction

298 strain also reached its maximum at 60°. Among the tested inclinations, II-60 and X-60 therefore showed
299 relative maxima in major direction unloading deformation. Fissure configuration also affected Poisson's
300 ratio. The unloading response was asymmetric between the major and minor principal stress directions.

301 **4. Failure patterns and crack distributions**

302 Viewed along the intermediate principal stress direction, failure was dominated by shear cracks
303 and accompanied by interlayer cracking (Fig. 14). Crack density was greater on the positive side of the
304 unloading direction than on the opposite side. This distribution is consistent with greater damage near
305 an excavation boundary. Figures 15–17 show failure patterns viewed along the minor principal stress
306 direction. All specimens developed some horizontal interlayer cracks because of the layered shale
307 structure. Many specimens also developed curved cracks. Circular marks at the face centers were
308 produced by AE sensor contact and residual couplant.

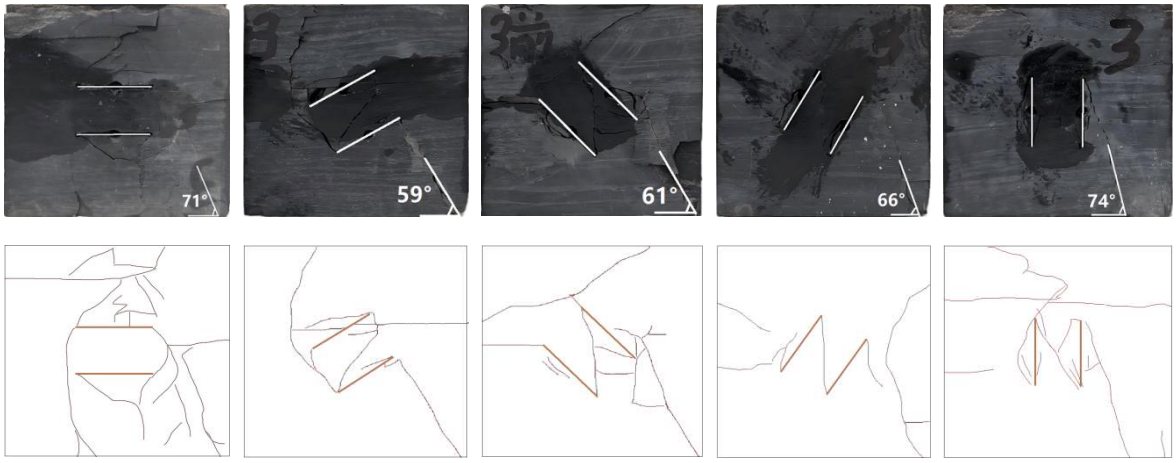


(a) Intact (b) II-45 (c) X-60 (d) XI-C

Figure 14. Failure patterns viewed along the intermediate principal stress direction.

309 4.1 Group II

310 Figure 15 shows the failure patterns of Group II viewed along the minor principal stress direction.



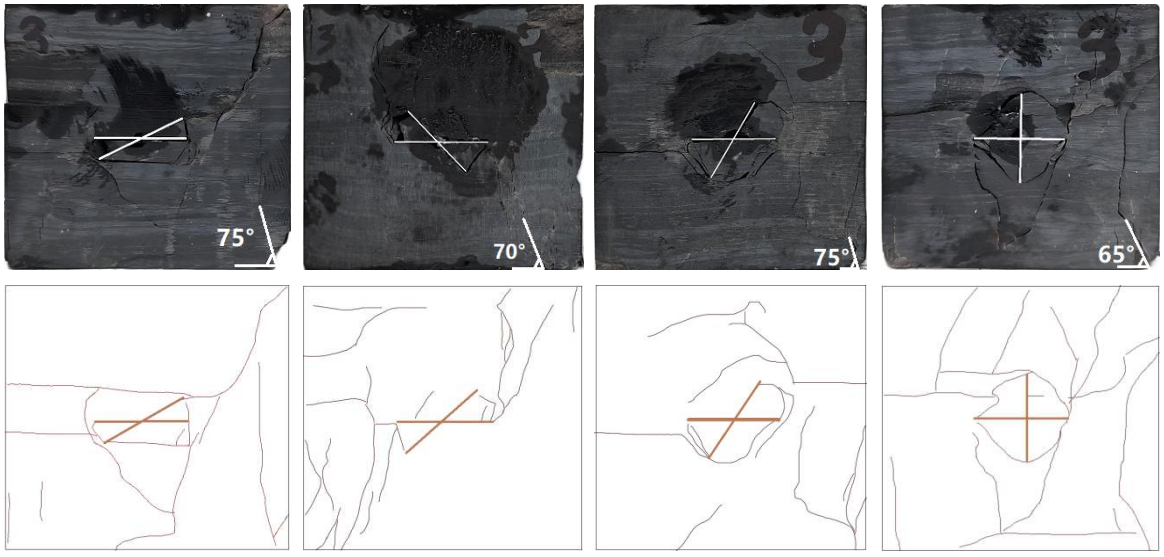
(a) II-0 (b) II-30 (c) II-45 (d) II-60 (e) II-90

Figure 15. Group II failure patterns viewed along the minor principal stress direction.

Most cracks were straight, although a few curved cracks formed near the preexisting fissures (Fig. 15). The specimen at 0° developed arch shaped cracks above and below the horizontal fissures. No crack connected the two fissures, and the failure angle was 71°. At inclinations from 30° to 90°, cracks coalesced between fissures and propagated from their tips to the specimen boundaries. The failure angle increased from 59° to 61°, 66°, and 74° as the inclination to bedding increased.

4.2 Group X

Figure 16 shows the failure patterns of Group X viewed along the minor principal stress direction.



(a) X-30 (b) X-45 (c) X-60 (d) X-90

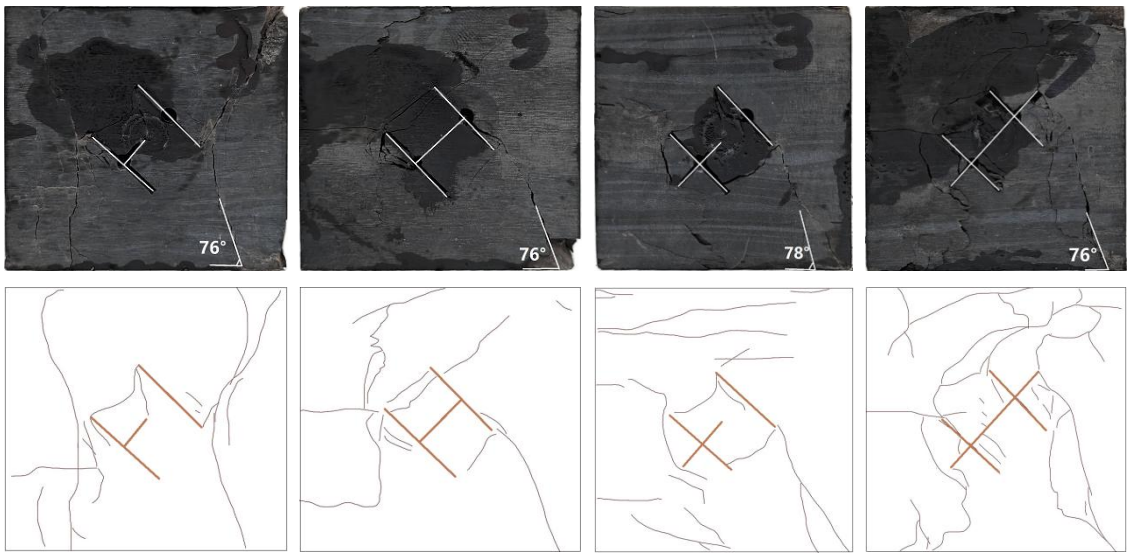
Figure 16. Group X failure patterns viewed along the minor principal stress direction.

Numerous curved cracks formed around the fissures in Group X (Fig. 16). They were most extensive in X-60, while the cruciform specimen X-90 showed the greatest fragmentation. X-30 contained two long horizontal interlayer cracks and a nearly rectangular closed crack pattern around the

fissures. Cracks connected the fissure ends, and failure angles remained near 70° in all specimens. Above 45°, the closed crack pattern became more circular and irregular as inclination increased. Every specimen also developed horizontal interlayer cracks. The crack envelope therefore changed from an elongated rectangle to a more equiaxed circle as the angle between the intersecting fissures increased. This change may reflect the positions and interactions of the fissure tips. The intersection angle changes the local mixed loading state and may influence crack deflection and coalescence. Numerical work on intersecting fissures has identified both straight and curved paths between adjacent tips [22].

4.3 Group XI

Figure 17 shows the failure patterns of Group XI viewed along the minor principal stress direction.



(a) XI-A (b) XI-B (c) XI-C (d) XI-D

Figure 17. Group XI failure patterns viewed along the minor principal stress direction.

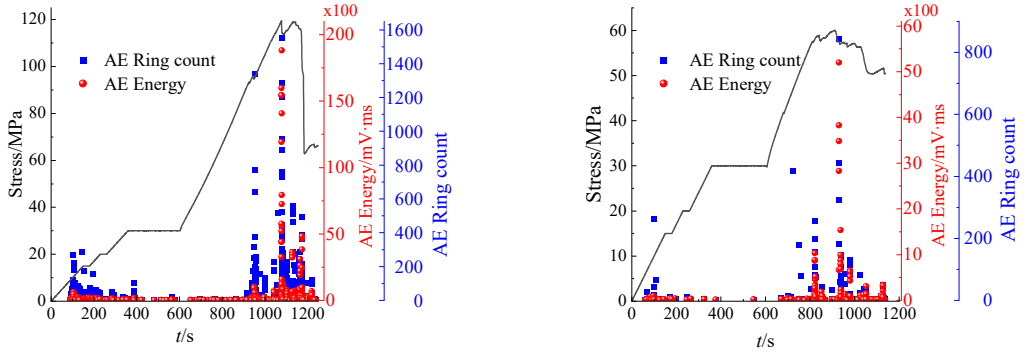
In Group XI, cracks from the ends of the two parallel fissures coalesced and reached the specimen boundaries (Fig. 17). Compared with II-45 in Fig. 15(c), the third fissure increased fragmentation. Cracks grew from the third fissure tips when that fissure extended beyond the parallel pair. Fragmentation increased with the length of the third fissure, while the failure angle remained near 76°. The third fissure therefore increased the failure angle from 61° in II-45 to about 76° in Group XI.

Final photographs showed that major cracks commonly passed through fissure tips, rock bridges, and bedding planes. These discontinuities jointly constrained the final paths. In Group II, the failure angle changed with fissure inclination. Group X developed more complex ring shaped patterns at larger inclinations. In Group XI, the third fissure tips participated in coalescence and increased local fragmentation. Fissure orientation, intersection geometry, and bedding may therefore act together to

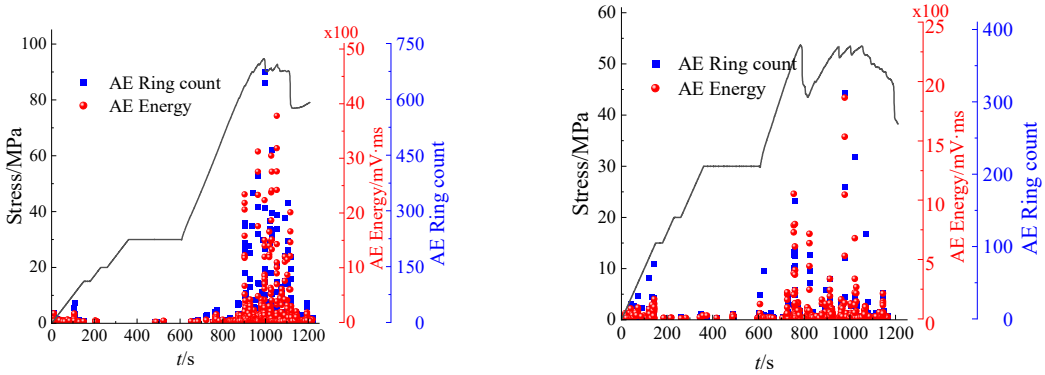
alter the macroscopic crack path. Cracking along bedding also indicates a possible influence of bedding strength and wave velocity anisotropy.

5. Acoustic emission characteristics

Figure 18 shows the AE response of representative specimens. The first stage comprised in situ stress loading. Ring down counts and energy varied within a limited range and first increased, then decreased. This response indicates compaction of natural fissures followed by stabilization after closure. The second stage comprised unloading and reloading in the minor principal stress direction from 15 MPa to 0 MPa and then to 0.5 MPa. Counts and energy remained stable, with only small fluctuations. Small new cracks may have formed, or closed natural cracks may have reopened during unloading. Weak plastic behavior appeared as a short nonlinear segment at the start of the third stage. It became more evident as the fissure configuration became more complex. In the third stage, displacement controlled loading in the major principal stress direction continued to failure. A short plastic segment was followed by closure of small cracks and a temporary return to a near elastic response. The internal structure then changed as the preexisting fissures closed and propagated. Ring down counts and energy rose rapidly and reached their maxima near failure. The intact specimen showed a pronounced AE threshold near 95 MPa, which was interpreted as a Kaiser effect.



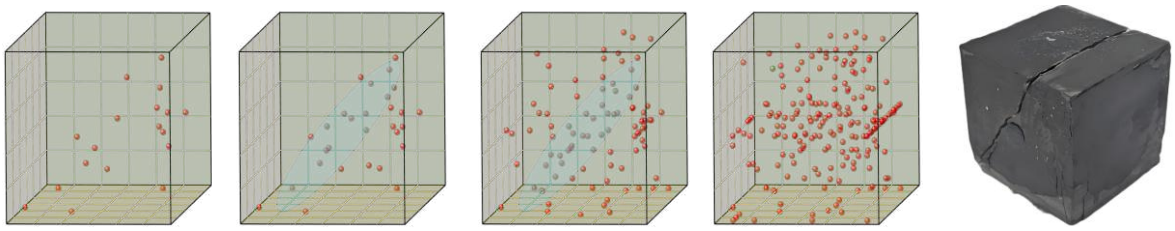
(a) Intact (b) II-45



(c) X-45 (d) XI-C

Figure 18. AE ring down counts and energy of representative specimens.

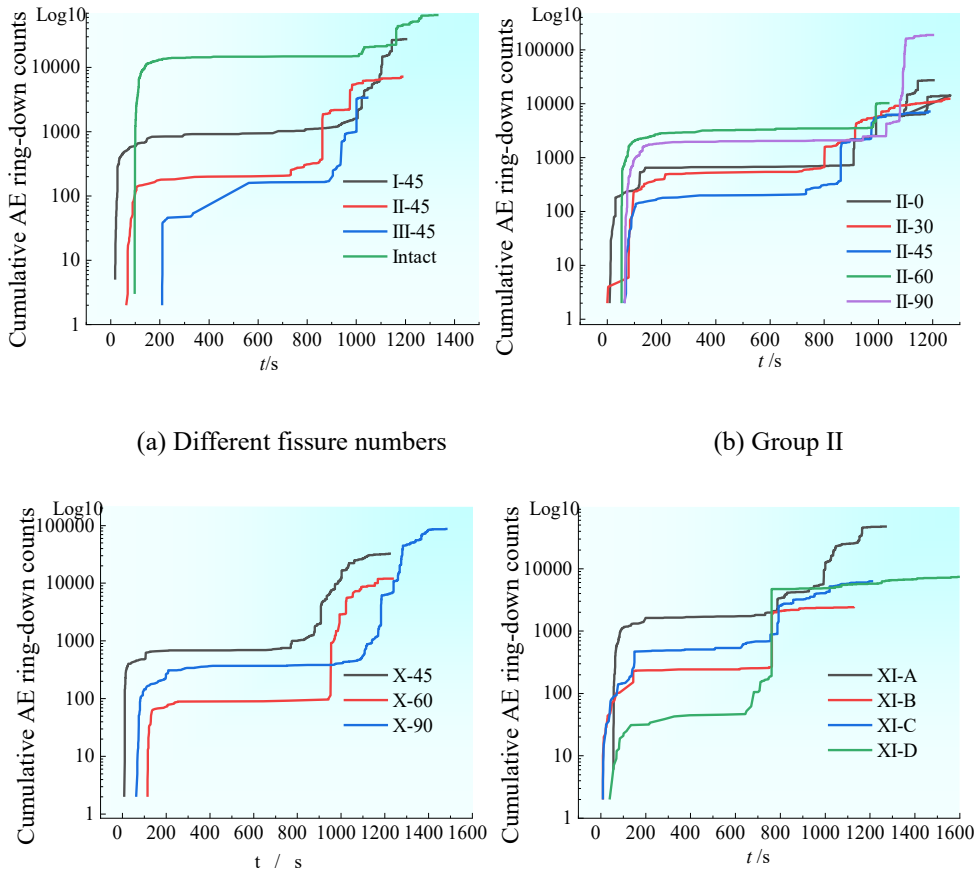
Figure 19 shows AE source locations during failure of the intact specimen. During in situ stress loading from 0 to 30 MPa, sparse events accompanied closure of natural cracks. Event locations remained stable during unloading and reloading, with only a small increase in number. At crack initiation, many events formed along a 45° diagonal. This pattern indicates progressive crack growth across the specimen diagonal. During failure, numerous irregular events reflected extensive internal crack propagation.



(a) In situ stress loading (b) Unloading–reloading (c) Crack initiation (d) Failure (e) Final failure photograph

Figure 19. AE source locations during failure of the intact specimen.

Figure 20 shows cumulative AE ring down counts over time. Counts increased rapidly during in situ stress loading as natural fissures compacted. From the start of unloading to crack initiation, the counts changed little while elastic strain energy accumulated. Counts then increased in steps from crack initiation to failure, consistent with crack opening and growth. Specimens with more complex configurations recorded fewer cumulative counts. This difference may reflect localized failure and frictional sliding along preexisting fissures.



(a) Different fissure numbers (b) Group II

(c) Group X (d) Group XI

Figure 20. Cumulative AE ring down counts of the specimens.

6. Conclusions

True triaxial unloading–reloading tests with AE monitoring were conducted on shale specimens with different fissure geometries. The stress path represented excavation unloading and subsequent initial support at a tunnel wall. The tests quantified how fissure number, inclination, configuration, and rock bridge continuity affected shale behavior.

(1) At a fissure inclination of 45°, increasing the fissure number from zero to three reduced peak strength from 119.4 to 44.7 MPa. The elastic modulus decreased from 12.06 to 4.72 GPa, and peak strain decreased overall from 0.88% to 0.46%. Multiple fissures therefore reduced stiffness, deformation capacity before peak stress, and peak strength. Residual strength did not decrease linearly because fissure closure and frictional sliding also influenced capacity after peak stress.

(2) The effect of inclination depended on fissure configuration. II-60 showed large unloading deformation but low peak strain and residual strength during final loading. In X-60, μ_{13} reached 0.42

and the residual strength ratio reached 0.92. In Group XI, μ_{13} was about 1.6–3.1 times μ_{12}. The specimens therefore showed a stronger response in the minor principal stress direction.

(3) The normalized stress drop ratio and the interval between the drop and failure described the magnitude and timing of local capacity loss. The specimens showed three processes: a drop followed by recovery and failure, failure without a distinct preceding drop, and a drop that coincided with failure.

(4) AE activity reflected the failure process. Counts rose rapidly during initial loading as natural fissures compacted. They changed little during unloading, then increased sharply with energy as failure approached. More complex fissure configurations produced fewer cumulative ring down counts. Final photographs showed that major cracks commonly passed through fissure tips, rock bridges, and bedding planes.

(5) Fissure configuration controlled the failure pattern. In Group II, the failure angle increased from 59° to 74° with inclination. In Group X, the crack envelope changed from nearly rectangular to ring shaped and became more fragmented. Adding a third fissure increased the failure angle from 61° in II-45 to about 76° in Group XI and intensified fragmentation. Under the tested conditions, fissure geometry and bedding jointly controlled strength, unloading deformation, AE development, and the final crack path.

Author contributions

Beiyi Dong: Methodology, investigation, formal analysis, and writing the original draft. Xinqiang Gao: Conceptualization, supervision, project administration, and review and editing. Dongliang Ji: Methodology, validation, and review and editing. Chao Kong: Resources, validation, and review and editing. Qian Yan: Investigation and data curation. Minghao Ruan: Investigation, data curation, and visualization.

Funding

This work was supported by the Hebei Provincial Science and Technology Program under Grant [24465001D] and the Science and Technology Project of China Railway 16th Bureau Group Co., Ltd. under Grant [YSLJX-KYJS-2024-002].

Competing interests

The authors report there are no competing interests to declare.

Declaration of generative AI use

Generative AI tools from OpenAI were used to assist with English translation and language editing. The authors reviewed and revised all resulting text and take full responsibility for the accuracy and integrity of the manuscript.

Data availability statement

The data that support the findings of this study are available from the corresponding author, Xinqiang Gao, upon reasonable request.

References

[1] Feng, F. et al. Investigation on the failure characteristics of fissured sandstone under true triaxial unloading and dynamic disturbance condition. *Chin. J. Rock Mech. Eng.* **44,** 618–637 (2025). https://doi.org/10.3724/1000-6915.jrme.2024.0583.

[2] Teng, J. Y., Tang, J. X., Wang, J. B. & Zhang, Y. N. The evolution law of the damage of bedded composite rock and its fractal characteristics. *Chin. J. Rock Mech. Eng.* **37(S1),** 3263–3278 (2018). https://doi.org/10.13722/j.cnki.jrme.2016.1397.

[3] Feng, F. et al. Effects of external dynamic disturbances and structural plane on rock fracturing around deep underground cavern. *Int. J. Coal Sci. Technol.* **9,** 15 (2022). https://doi.org/10.1007/s40789-022-00487-z.

[4] Lu, W. B., Zhou, C. B., Chen, M., Jin, L. & Yan, P. Research on transient characteristics of excavation unloading. *Chin. J. Rock Mech. Eng.* **27,** 2184–2192 (2008).

[5] Zhang, W. J., Lu, W. B., Yang, J. H., Yan, P. & Chen, M. Cracking characteristics and influential factors of surrounding rocks induced by excavation unloading in deep tunnel. *Rock Soil Mech.* **34,** 2690–2698 (2013).

[6] Ding, X. et al. Experimental study on mechanical properties and acoustic emission of gas bearing coal under single surface unloading path. *J. China Coal Soc.* **48,** 2194–2206 (2023). https://doi.org/10.13225/j.cnki.jccs.2023.0038.

[7] Rong, H. Y., Li, G. C., Zhao, G. M., Liang, D. X. & Liang, J. L. True triaxial test study on mechanical properties of deep rock mass in different stress paths. *J. China Coal Soc.* **45,** 3140–3149 (2020). https://doi.org/10.13225/j.cnki.jccs.2019.0891.

[8] Xu, W. S. et al. Test study on true triaxial loading and unloading for marble with unloaded single face. *J. Southwest Jiaotong Univ.* **54,** 526–534 (2019). https://doi.org/10.3969/j.issn.0258-2724.20180542.

[9] Hou, G. Y., Li, X. R., Zhang, Z. D., Liang, H. Y. & Zhang, J. C. Experimental system for simulating excavation unloading process of rock around roadway by using small cylindrical hollow specimen. *Chin. J. Rock Mech. Eng.* **36,** 2136–2145 (2017). https://doi.org/10.13722/j.cnki.jrme.2016.1585.

[10] Wong, L. N. Y. & Einstein, H. H. Systematic evaluation of cracking behavior in specimens containing single flaws under uniaxial compression. *Int. J. Rock Mech. Min. Sci.* **46,** 239–249 (2009). https://doi.org/10.1016/j.ijrmms.2008.03.006.

[11] Yang, S. Q. & Jing, H. W. Strength failure and crack coalescence behavior of brittle sandstone samples containing a single fissure under uniaxial compression. *Int. J. Fract.* **168,** 227–250 (2011). https://doi.org/10.1007/s10704-010-9576-4.

[12] Wang, H., Dyskin, A., Pasternak, E. & Dight, P. 3D crack growth in biaxial compression: influence of shape and inclination of initial cracks. *Rock Mech. Rock Eng.* **53,** 3161–3183 (2020). https://doi.org/10.1007/s00603-020-02089-0.

[13] Pakzad, R., Wang, S. & Sloan, S. Numerical study of the failure response and fracture propagation for rock specimens with preexisting flaws under compression. *Int. J. Geomech.* **18,** 04018070 (2018). https://doi.org/10.1061/(ASCE)GM.1943-5622.0001172.

[14] Reik, G. & Zacas, M. Strength and deformation characteristics of jointed media in true triaxial compression. *Int. J. Rock Mech. Min. Sci. Geomech. Abstr.* **15,** 295–303 (1978). https://doi.org/10.1016/0148-9062(78)91470-5.

[15] Thaweeboon, S., Dasri, R., Sartkaew, S. & Fuenkajorn, K. Strength and deformability of small scale rock mass models under large confinements. *Bull. Eng. Geol. Environ.* **76,** 1129–1141 (2017). https://doi.org/10.1007/s10064-016-0871-9.

[16] Li, Z., Wang, L. & Li, W. Mechanical behavior and fracture characteristics of rock with prefabricated crack under different triaxial stress conditions. *Minerals* **12,** 673 (2022). https://doi.org/10.3390/min12060673.

[17] Chang, X., Zhang, X., Dang, F., Zhang, B. & Chang, F. Failure behavior of sandstone specimens containing a single flaw under true triaxial compression. *Rock Mech. Rock Eng.* **55,** 2111–2127 (2022). https://doi.org/10.1007/s00603-021-02761-z.

[18] Yang, S. Q. et al. Three dimensional failure behavior and cracking mechanism of rectangular solid sandstone containing a single fissure under triaxial compression. *Rock Mech. Bull.* **1,** 100008 (2022). https://doi.org/10.1016/j.rockmb.2022.100008.

[19] Feng, F. et al. True triaxial unloading test on the mechanical behaviors of sandstone: effects of the intermediate principal stress and structural plane. *J. Rock Mech. Geotech. Eng.* **17,** 2208–2226 (2025). https://doi.org/10.1016/j.jrmge.2024.04.005.

[20] Zhang, X. W., Feng, X. T., Kong, R., Wang, G. & Peng, S. Key technology in development of true triaxial apparatus to determine stress–strain curves for hard rocks. *Chin. J. Rock Mech. Eng.* **36,** 2629–2640 (2017). https://doi.org/10.13722/j.cnki.jrme.2017.1215.

[21] Zhang, J. R. et al. Study on stability of excavation face of long span highway tunnel in soil stratum in western Yunnan. *China J. Highw. Transp.* **38,** 242–254 (2025). https://doi.org/10.19721/j.cnki.1001-7372.2025.09.018.

[22] Dai, B., Chen, Y., Zhao, G., Liang, W. & Wu, H. A numerical study on the crack development behavior of rock like material containing two intersecting flaws. *Mathematics* **7,** 1223 (2019). https://doi.org/10.3390/math7121223.